Frequency-Dependent Squeezing from a Detuned Squeezer

Jonas Junker,* Dennis Wilken, Nived Johny, Daniel Steinmeyer, and Michèle Heurs
Max Planck Institute for Gravitational Physics (Albert Einstein Institute), and Institute for Gravitational Physics, Leibniz Universität Hannover, Callinstraße 38, 30167 Hannover, Germany

(Received 3 March 2022; accepted 31 May 2022; published 14 July 2022)

Frequency-dependent squeezing is a promising technique to overcome the standard quantum limit in optomechanical force measurements, e.g., gravitational wave detectors. For the first time, we show that frequency-dependent squeezing can be produced by detuning an optical parametric oscillator from resonance. Its frequency-dependent Wigner function is reconstructed quantum tomographically and exhibits a rotation by 39°, along which the noise is reduced by up to 5.5 dB. Our setup is suitable for realizing effective negative-mass oscillators required for coherent quantum noise cancellation.

DOI: 10.1103/PhysRevLett.129.033602

According to quantum mechanics, the continuous measurement of an object's position creates a random quantum backaction perturbation on its momentum. This backaction noise, together with the shot noise, fundamentally limits the precision in ultrasensitive force measurements, e.g., in cavity optomechanics [1] or gravitational wave detection [2–5]. The sensitivity limit imposed by backaction noise and shot noise is referred to as the standard quantum limit (SQL) of interferometry. Previous experiments measured mechanical motions with an imprecision below the SQL [6,7] observed quantum backaction [8–12] or demonstrated sensitivities near the SQL [10,13–15]. To reduce or even evade the effect of quantum backaction and to overcome the SQL, various quantum nondemolition techniques have been proposed, e.g., variational readout [16,17], two-tone measurements [18–20], stroboscopic measurements [21,22], the optical spring effect [23], or the use of Kerr media [24].

The SQL can also be beaten by the injection of frequency-dependent squeezing. For a lossless and nondetuned interferometer, the squeezing angle is optimized for each frequency ω with $\theta(\omega) = -\mathrm{arccot}\mathcal{K}(\omega)$, and Kimble factor $\mathcal{K}$ [16]. Then, the sensitivity can be improved by e^{-2r} with squeezing factor r in a broad frequency band [16]. Typically, frequency-dependent squeezing is generated by reflecting frequency-independent squeezed light off a detuned filter cavity [25–28]. However, frequency-dependent squeezing of this form cannot entirely evade quantum backaction noise because r is frequency-independent [16].

In contrast, the entire backaction noise can be evaded by using an effective negative-mass oscillator [29–31]. In the cascaded all-optical realization of coherent quantum noise cancellation [31,32], the optomechanical system and the effective negative-mass oscillator are independent subsystems [33]. There, the effective negative-mass oscillator produces a state that effectively exhibits frequency-dependent squeezing to counteract the effect of the disturbing ponderomotive squeezing of the optomechanical oscillator [33]. The squeezing, generated by this effective negative-mass oscillator, exhibits both a frequency-dependent rotation angle $\theta(\omega)$ and squeezing factor $r(\omega)$. Ideally, this state entirely evades backaction noise and is equal to the *inversely input squeezed* state [16]. To realize a well-matched effective negative-mass oscillator, a complicated coupled system, using a beam splitter process and a down-conversion interaction, has been studied in detail [32]. Instead of this complex system, in this Letter, we propose using a simpler and elegant alternative as an effective negative-mass oscillator.

We report on the generation of frequency-dependent squeezing using a detuned optical parametric oscillator (OPO). We show that the output state of this squeezer exhibits a frequency-dependent squeezing factor and rotation angle. We analyze the state by tomographically reconstructing its Wigner function at different measurement frequencies. The obtained Wigner functions agree well with our measured and simulated noise spectra. Our findings are relevant for optomechanical force measurements, e.g., gravitational wave detectors, limited by quantum backaction noise.

The system is described theoretically by applying the input-output formalism [34,35] on a linear lossless OPO, shown in Fig. 1. The interaction Hamiltonian for this nonclassical light source is

$$H = \frac{i\hbar g}{2}(\hat{a}^2 - \hat{a}^{\dagger 2}), \tag{1}$$

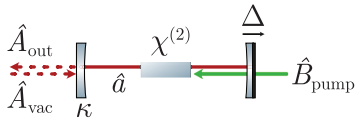

FIG. 1. Schematic of the optical parametric oscillator with decay rate κ and intracavity field $\hat{a}$. The $\chi^{(2)}$ medium is pumped with $\hat{B}_{\mathrm{pump}}$. When the cavity is detuned by Δ from its resonance, the vacuum fluctuations $\hat{A}_{\mathrm{vac}}$ are converted into an output field $\hat{A}_{\mathrm{out}}$ exhibiting frequency-dependent squeezing.

where we assume an undepleted pump field $\hat{B}_{\mathrm{pump}}$. The coupling strength of the down-conversion process is given by $g = 2\chi^{(2)}\hat{B}_{\mathrm{pump}}$, where $\chi^{(2)}$ is the nonlinear coefficient of the down-conversion process. The pump oscillates with ω_p and does not exceed the threshold of the OPO. Vacuum fluctuations $\hat{A}_{\mathrm{vac}}$ couple to the intracavity field through the input coupling mirror. The derivative of the circulating intracavity field is

$$\dot{\hat{a}} = i\hat{a}\Delta - \hat{a}\kappa + \hat{a}^{\dagger}g + \hat{A}_{\mathrm{vac}}\sqrt{2\kappa}. \tag{2}$$

We define the detuning Δ as the difference between cavity resonance frequency and fundamental frequency $\omega_0 = \omega_p/2$. The authors in [36] also considered the theory of a detuned but doubly resonant OPO (but they did not consider the frequency-dependent output state rotation). However, in many other publications [37–39], Δ is set to 0. The cavity has a decay rate κ, where $\kappa = 2\pi\nu/\mathcal{F}$ with finesse $\mathcal{F}$, free spectral range (FSR) $\nu = c/L$, and round-trip length L. We can decompose the field operators $\hat{a}$ in a constant and a fluctuating term in the form $\hat{a} = \langle\hat{a}\rangle + \delta\hat{a}$. Then, Eq. (2) can be solved in the frequency domain as in [40,41] using the input-output theory [34,35] for the fluctuating terms $\delta\hat{a}(\omega)$ and $\delta\hat{a}^{\dagger}(\omega)$. After applying the cavity boundary condition [42], we can compute the fluctuating part of the output field $\delta\hat{A}_{\mathrm{out}} = \sqrt{2\kappa}\delta\hat{a} - \delta\hat{A}_{\mathrm{vac}}$. The fluctuations of the output amplitude and phase quadrature are $\delta\hat{X}_1 = \delta\hat{A}_{\mathrm{out}} + \delta\hat{A}^{\dagger}_{\mathrm{out}}$ and $\delta\hat{X}_2 = i(\delta\hat{A}_{\mathrm{out}} - \delta\hat{A}^{\dagger}_{\mathrm{out}})$, respectively.

To characterize the output state, it is convenient to derive the symmetrized covariance matrix of the output state. It contains the spectral densities and is defined by $\sigma_{kl} = \frac{1}{2}\langle\delta\hat{X}_k\delta\hat{X}_l + \delta\hat{X}_l\delta\hat{X}_k\rangle - \langle\delta\hat{X}_l\rangle\langle\delta\hat{X}_k\rangle$, where $\delta\boldsymbol{X} = (\delta\hat{X}_1, \delta\hat{X}_2)$. When assuming an input variance for the vacuum field of $V_{\mathrm{vac}} = 1$, the covariance matrix is

$$\begin{aligned}
\sigma_{11} &= 1 + \frac{4g\kappa(|\chi^{+}|^2 - \Delta^2)}{|\Delta + \chi^{+}\chi^{-}|^2}, \\
\sigma_{22} &= 1 - \frac{4g\kappa(|\chi^{-}|^2 - \Delta^2)}{|\Delta + \chi^{+}\chi^{-}|^2}, \\
\sigma_{12} &= \sigma_{21} = -\frac{8g\kappa^2\Delta}{|\Delta + \chi^{+}\chi^{-}|^2}.
\end{aligned} \tag{3}$$

Here, we have introduced $\chi^{\pm} = \kappa + i\omega \pm g$. For nonzero detuning $\Delta \neq 0$, we obtain nonvanishing off-diagonal elements of $\boldsymbol{\sigma}$. These entries arise from the rotation of the output state in phase space. Hence, the rotation depends on the detuning Δ and the measurement sideband frequency ω.

The covariance matrix $\boldsymbol{\sigma}$ describes a pure state because we consider a lossless OPO. Passive optical losses will degrade the squeezed output state. When the state experiences power losses l, corresponding to an efficiency $\eta = 1 - l$, the lossy covariance is $\boldsymbol{\sigma_l} = \eta\boldsymbol{\sigma} + (1-\eta)\mathrm{I}_2$, with I_2 being the 2×2 identity matrix.

This state can be phase sensitively detected with a balanced homodyne detector (HD), where it interferes with a local oscillator (LO) at frequency ω_0. The phase difference ψ between LO and output state defines the detection angle and, accordingly, the projection axis for the measurement. The measurement result of the HD corresponds to $\tilde{\sigma}_{11}(\psi)$, with

$$\tilde{\boldsymbol{\sigma}}(\psi) = \boldsymbol{R}^{\top}(\psi)\boldsymbol{\sigma_l}\boldsymbol{R}(\psi), \tag{4}$$

with rotation matrix $\boldsymbol{R}(\psi)$.

At $\omega = 0$, a specific detection angle ψ_0 diagonalizes $\tilde{\boldsymbol{\sigma}}(\psi_0)$ and maximized the measurable squeezing and antisqueezing values. This specific angle ψ_0 is

$$\psi_0 = -\frac{1}{2}\arctan\frac{2\kappa\Delta}{\Delta^2 - \kappa^2 - g^2}. \tag{5}$$

However, for measurement frequencies $\omega \neq 0$, $\tilde{\boldsymbol{\sigma}}(\psi_0)$ is not diagonal anymore. It still can be diagonalized with a frequency-dependent detection angle $\psi_{\boldsymbol{\omega}}$. The rotation angle $\theta(\omega)$ of the quadrature distribution in phase space is

$$\theta(\omega) = \psi_0 - \psi_{\boldsymbol{\omega}} = \psi_0 + \frac{1}{2}\arctan\frac{2\kappa\Delta}{\Delta^2 - \kappa^2 - g^2 - \omega^2}. \tag{6}$$

This shows again that the state rotation depends on the measurement frequency ω, indicating frequency-dependent squeezing. When changing the sign of Δ, the rotation direction flips because of the off-diagonal elements in Eq. (3). Thus, in the context of coherent quantum noise cancellation, the sign of Δ defines the positive or negative energy character of the oscillator.

A noisy detection angle ψ at the HD degrades the squeezing measurements. Assuming normally distributed fluctuations with a small standard deviation of $\delta\psi$ [38], the detected noise level is

$$\tilde{\sigma}^{\mathrm{det}}_{11} = \tilde{\sigma}_{11}\cos^2(\delta\psi) + \tilde{\sigma}_{22}\sin^2(\delta\psi) + \tilde{\sigma}_{12}\sin(2\delta\psi). \tag{7}$$

To aid understanding, the detuned OPOs' essential features are shown in Fig. 2. Here, the output state's noise distribution is depicted by an ellipse in phase space.

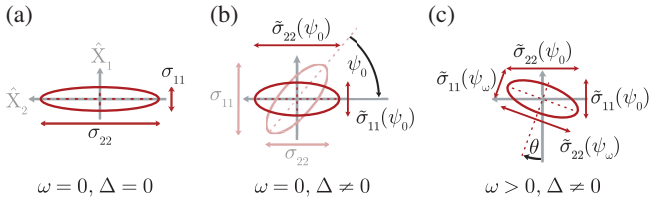

FIG. 2. The output state of the OPO is represented by the noise ellipse in phase space. In (a) the resonant OPO generates a noise ellipse with diagonal covariance matrix $\boldsymbol{\sigma}$ at baseband ($\omega = 0$). In (b) the OPO is detuned by Δ, generating a noise ellipse having a nondiagonal $\boldsymbol{\sigma}$. According to Eq. (4), the covariance matrix can be rotated to $\tilde{\boldsymbol{\sigma}}(\psi_0)$, which is diagonal. In (c) for a larger measurement frequency $\omega > 0$ the noise ellipse given by $\tilde{\boldsymbol{\sigma}}(\psi_0)$ has rotated by θ. Now, the maximum squeezing and antisqueezing levels can be obtained from $\tilde{\sigma}_{11}(\psi_{\boldsymbol{\omega}})$ and $\tilde{\sigma}_{22}(\psi_{\boldsymbol{\omega}})$.

Figure 2(a) shows the ordinary case of a resonant OPO at a measurement frequency $\omega = 0$. The pump's phase is set to deamplification of $\delta\hat{X}_1$, and no state rotation can be seen. In (b), the OPO is detuned ($\Delta \neq 0$) but the measurement frequency is still at $\omega = 0$. The cavity phase response leads to a rotation of the ellipse by ψ_0, represented by the whitened state with nondiagonal covariance matrix $\boldsymbol{\sigma}$. After using Eq. (4), the diagonalized state $\tilde{\boldsymbol{\sigma}}(\psi_0)$ is depicted, with main diagonal elements $\tilde{\sigma}_{11}(\psi_0)$ and $\tilde{\sigma}_{22}(\psi_0)$. Because of the detuning, the squeezing and antisqueezing levels $\tilde{\sigma}_{11}(\psi_0)$ and $\tilde{\sigma}_{22}(\psi_0)$ are reduced compared to (a). In (c), the OPO is still detuned but now the measurement frequency has changed. Depending on the actual measurement frequency ω, positive and negative sideband frequencies accumulate nonsymmetrical phases. The main consequence is a frequency-dependent squeezing angle θ. Additionally, the maximum squeezing and antisqueezing levels are also frequency-dependent and they are depicted by $\tilde{\sigma}_{11}(\psi_{\boldsymbol{\omega}})$ and $\tilde{\sigma}_{22}(\psi_{\boldsymbol{\omega}})$.

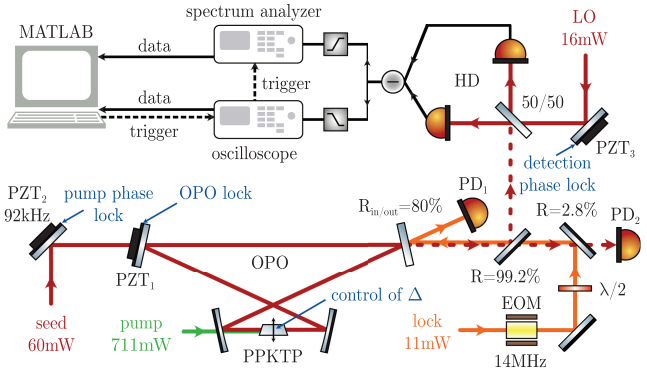

FIG. 3. Experimental setup consisting of the detuned OPO that generates a frequency-dependent squeezed state (bottom) and the HD with the data acquisition for reconstructing the state's Wigner function (top). The actuators of the locking loops are indicated in blue.

The schematic of our experimental setup is shown in Fig. 3. The core element of our free-space OPO is a 1 mm × 2 mm × 10 mm nonlinear periodically poled potassium titanyl phosphate (PPKTP) type I crystal. It is temperature-controlled to 31 °C to ensure phase matching for the s-polarized down-conversion process. The 0.5° trapezoidal-shaped crystal is placed in a four mirror cavity topology with an FSR of $\nu = 197$ MHz. The plane input (front) mirror has a power reflectivity of $R_{\text{in/out}} = 80\%$. The plane rear mirror and the curved mirrors are highly reflective for the fundamental wavelength of 1064 nm and antireflective for the 532 nm green pump light.

We want to lock the OPO cavity to an arbitrary detuning Δ. This is realized by using perpendicularly polarized fields for locking and pumping using the cavity's adjustable birefringence. The refractive index of the PPKTP crystal is polarization- and temperature-dependent. Its trapezoidal shape allows us to change the crystal's effective length by shifting it perpendicular to the beam axis and parallel to the cavity plane. Thus, we can adjust the frequency difference between s-polarization and p-polarization resonances. Fine-tuning can be achieved by changing the crystal's temperature (a frequency difference of 1 MHz corresponds roughly to a temperature change of 0.1 °C). Here, the effect on the nonlinear efficiency can be neglected. For the measurements presented in this Letter, the detuning was set to $\Delta = -2\pi \times 3.6$ MHz.

We inject a p-polarized 14 MHz phase-modulated field into the cavity to stabilize to the chosen detuning via Pound-Drever-Hall locking. For locking on resonance, an s-polarized beam is used. The locking field is sent in counterpropagatingly to avoid cross-coupling and is detected in reflection of the OPO by photodetector PD_1. After demodulation and filtering, the control signal is fed back to the piezoelectric transducer PZT_1 clamped onto the rear mirror.

The squeezing angle needs to be actively stabilized. Therefore, we inject a seed through the rear highly reflective mirror, which is phase-modulated at 92 kHz by PZT_2. This field serves as a reference for the frequency-dependent squeezing. By detecting and demodulating a fraction of the seed field behind the $R = 99.2\%$ mirror on PD_2, we are able to lock to the pump phase. The locking point is chosen such that the amplitude quadrature fluctuations are minimized. Technically, the seed displaces the squeezed vacuum converting it into a bright squeezed state.

The generated state is detected by a balanced HD scheme. Technical noise of the seed would dominate the measurement at baseband frequencies. Therefore, we take our measurements around the first FSR of the OPO at ν. The covariance matrix will be identical at frequencies corresponding to higher FSRs $\tilde{\boldsymbol{\sigma}}(\psi, \omega) = \tilde{\boldsymbol{\sigma}}(\psi, \omega + n\nu)$, $n \in \mathbb{Z}$, because of the spectral periodicity of the OPO's response. This approach has two advantages: First, measurement frequencies both above and below the resonance

frequency can be resolved, and second, experimental challenges of measuring squeezing at baseband can be avoided. The phase difference between the strong LO and the bright squeezed field determines the detection angle and can be changed with PZT_3. In order to measure the squeezing spectrum at a certain detection angle, the phase difference is usually stabilized at this angle. However, even with a swept LO, a full tomographic state reconstruction is possible, as can be seen in the following.

We record the homodyne projections for a measurement time of 1 s per measurement frequency while the LO phase is ramped for our tomographic reconstructions. The low-frequency output of the HD is recorded by an oscilloscope and shows the interference between seed and LO. The high-frequency output is demodulated at the measurement frequency around ω using a spectrum analyzer [Keysight, N9020A MXA] and recorded as amplitude time series on a computer. This signal exhibits the quadrature fluctuations of the squeezed state scaled with the amplitude of the LO. The data acquisition is realized with a MATLAB script that triggers and stores the measurement for each frequency bin.

The Wigner function is tomographically reconstructed in four steps. First, we use the low-frequency interference signal to map each voltage amplitude recorded by the spectrum analyzer to a detection angle between 0° and 180°. Second, the amplitudes are sorted into 180 angular bins depending on their detection angle. Third, for each angular bin, all amplitudes are distributed in a histogram with 201 bars. Now the data are stored in a 201×180 array. Fourth, the array is inversely Radon transformed by using the built-in MATLAB function *iradon*, leading to the filtered back-projected Wigner function [43]. This algorithm is repeated for a vacuum state measurement to normalize the Wigner function. The Wigner function is connected to the previously derived covariance matrix. Using the first moments $d_j = \langle(\hat{X}_1, \hat{X}_2)\rangle$ of the state, the Wigner function reads [44]

$$W(\boldsymbol{X}) = \frac{1}{\pi\sqrt{\det(\boldsymbol{\sigma})}} e^{-(\boldsymbol{X}-\boldsymbol{d})^\top \boldsymbol{\sigma}^{-1}(\boldsymbol{X}-\boldsymbol{d})}. \tag{8}$$

Before characterizing the detuned OPO, we analyze the performance of the resonant OPO. We generate an amplitude quadrature squeezed state by locking the pump's phase to the seed. From the measurements of the (squeezed) amplitude quadrature and the antisqueezed phase quadrature for different pump powers, we obtained $\delta\psi = 15$ mrad phase noise and a total efficiency $\eta = 92.8\%$ the same way as in [45]. At a pump power of 711 mW, we observed -9.8 dB of squeezing and 15.3 dB of antisqueezing at the first FSR, which corresponds to $g = -2\pi \times 2.3$ MHz. In separate measurements, we determined the OPO decay rate $\kappa = 2\pi \times 3.2$ MHz, the escape efficiency of the OPO $\eta_{\mathrm{esc}} = 98.3\%$, the propagation efficiency $\eta_{\mathrm{prop}} = 99.0\%$, and the homodyne efficiency $\eta_{\mathrm{hd}} = 97.6\%$. From these measurements, we estimated the quantum efficiency of the HD with $\eta_{\mathrm{qe}} = \eta/(\eta_{\mathrm{esc}}\eta_{\mathrm{prop}}\eta_{\mathrm{hd}}) > 97.6\%$ as in [46].

In a second step, we stabilized the OPO with a detuning of $\Delta = -2\pi \times 3.6$ MHz and again produced an amplitude quadrature squeezed state. We investigated the frequency behavior of the state with the tomographic reconstruction method described above. In the top row of Fig. 4, three examples for reconstructed Wigner functions are shown for the frequencies 194, 197, and 203 MHz. An animation showing the rotation over the entire spectrum can be found in the Supplemental Material [47]. In the middle row, we show the measured maximal and minimal noise levels, and the rotation angle (both with estimated absolute errors). These data points are obtained by fitting the reconstructed Wigner distribution to Eq. (8). Equation (6) yields the solid

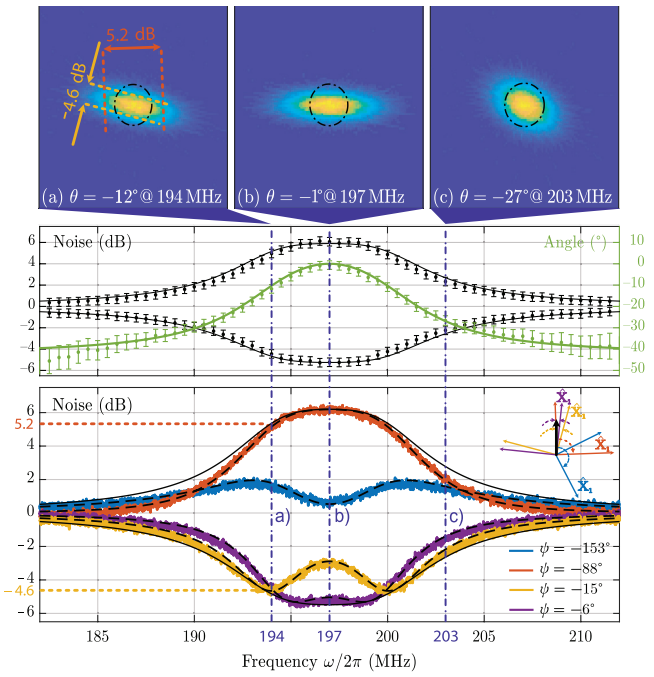

FIG. 4. Top row: Tomographically reconstructed Wigner functions for the frequencies (a) 194 MHz, (b) 197 MHz, and (c) 203 MHz; see Supplemental Material [47] for more reconstructions. The dashed circles indicate the shot noise levels as a reference. Middle row: Rotation angles, squeezing, and antisqueezing values obtained from fitting a two-dimensional Gaussian function to our reconstructed distributions. The solid green trace was plotted using Eq. (6). The solid black traces show simulations when the detection angle is aligned to the maximum squeezing and antisqueezing axes at each measurement frequency, $\tilde{\sigma}_{11}(\psi_\omega)$ and $\tilde{\sigma}_{22}(\psi_\omega)$, respectively. Bottom row: The widths of the Wigner function are measured at four different detection angles of the HD shown by the colored traces with a spectrum analyzer ([Keysight, N9020A MXA]; resolution bandwidth (RBW), 100 kHz; video bandwidth (VBW), 100 Hz; sweep time, 5 s; average, 10). The black dashed traces are simulations of $\tilde{\sigma}_{11}(\psi - \psi_0)$ from Eq. (7) for these four specific angles.

curves for $\theta(\omega)$ and ψ_ω. Note that in the upper two rows, the coupling strength ($g = -2\pi \times 2.2$ MHz) was slightly reduced with respect to the measurements in the bottom row, as the measurements were taken at different times. In the bottom row, we show recorded spectra for different detection angles ψ. Here, each colored trace corresponds to a width of the Wigner function under a specified and stabilized detection phase ψ of the LO (0° corresponds to detecting the amplitude quadrature). The chosen angles represent four qualitatively different spectra. All measurements are normalized to shot noise. The electronic dark noise was 14.3 to 15.0 dB below the shot noise and was subtracted from the data. The angles are obtained from the fits (black dashed traces), which are based on Eq. (7). When choosing the optimal detection angle at all frequencies, we get the black solid envelop traces.

We observed frequency-dependent squeezing over the full measurement band of 30 MHz. At the first FSR at 197 MHz, the state rotates from $\theta = 0°$ to $\theta = 39°$ clockwise toward higher and lower frequencies (see Supplemental Material [47]). This rotation symmetry can only be seen at higher FSRs and was, to our knowledge, not observed before. The rotation angle θ agrees with the angle θ_0 determined to diagonalize the output covariance matrix at each measurement frequency; see Eq. (4). We detected a maximum squeezing of −5.5 dB and a maximum antisqueezing of 6.2 dB at the first FSR. These noise values match the independently measured and reconstructed Wigner functions, which validates our tomographic reconstruction method. The detuned OPO requires larger coupling strengths than the resonant OPO to reach equivalent squeezing values. This does not imply any additional losses. Compared to the resonant case, the pump threshold changed from $g_{\mathrm{thr}} = -2\pi \times 3.2$ MHz to $-2\pi \times 4.8$ MHz for the detuned case.

The relevant parameter defining the shape of the Wigner function of the output state is the relative detuning $\tilde{\Delta} = |\Delta|/\kappa$. In fact, when $\tilde{\Delta}$ increases, the maximum rotation angle increases as well. For a given pump power, the maximum squeezing level reduces for larger detunings. Our choice for $\tilde{\Delta} = |-3.6\ \mathrm{MHz}|/3.2\ \mathrm{MHz} = 1.125$ is a trade-off to achieve a state rotation of roughly 45° (required for the inversely input squeezed state [16]) and a decent squeezing level. For a large detuning $\tilde{\Delta} \gg 1$, the state experiences a rotation of 90°. However, the squeezing will vanish then.

Finally, we discuss the applicability of the detuned OPO to enhance sub-SQL measurement sensitivities. In gravitational wave detectors, the filter cavities require very low linewidths of hundreds of Hertz to rotate the squeezing over the detector's measurement band. Instead, building a detuned squeezer with equally low linewidth seems to be technically very challenging. Because of the residual parasitic reflections of the crystal, the detuned squeezer's cavity length would have to be even longer than that of the filter cavities. Moreover, to ensure a sufficiently large escape efficiency, the cavity finesse would need to be reduced. However, using our detuned squeezer approach (instead of the usual resonant squeezer) can serve as a phase-rotation correction mechanism in addition to the filter cavities. This is especially relevant for systems dominantly limited by quantum backaction noise, such as the low-frequency Einstein Telescope [48,49]. Other experiments in the field of cavity optomechanics have begun to observe backaction noise due to quantum radiation pressure noise [8–10]. Using a detuned OPO could be an approximate but simple and promising approach to realize an effective negative-mass oscillator to cancel quantum backaction noise [32]. However, experimentally applying the detuned OPO to an optomechanical system requires sophisticated parameter matching. We plan to further investigate the detuned OPO as an effective negative-mass oscillator for coherent quantum noise cancellation in the future.

We have demonstrated the generation and quantum tomographic reconstruction of frequency-dependent squeezed states from a detuned OPO. The observed squeezed state rotates by 39° for increasing frequencies until it is amplitude quadrature squeezed at the first FSR of 197 MHz. For frequencies larger than the first FSR, the state rotates backward by −39°. The state exhibits maximum squeezing and antisqueezing levels of −5.5 and 6.2 dB, with a measurement efficiency of $\eta = 92.8\%$. The detuned OPO provides a simple realization for the required effective negative-mass oscillator in quantum backaction evasion schemes, such as coherent quantum noise cancellation.

We thank Klemens Hammerer for insightful discussions. This work was funded by the Deutsche Forschungsgemeinschaft (Excellence PhoenixD (EXC 2122, Project ID 390833453), Excellence QuantumFrontiers (EXC 2123, Project ID 390837967), GRK 1991, OE 177/ 10-1).

*Corresponding author.
jonas.junker@aei.mpg.de

[1] M. Aspelmeyer, T. J. Kippenberg, and F. Marquardt, Rev. Mod. Phys. **86**, 1391 (2014).
[2] C. M. Caves, Phys. Rev. Lett. **45**, 75 (1980).
[3] A. A. Clerk, M. H. Devoret, S. M. Girvin, F. Marquardt, and R. J. Schoelkopf, Rev. Mod. Phys. **82**, 1155 (2010).
[4] H. Yu *et al.* (LIGO Scientific Collaboration), Nature (London) **583**, 43 (2020).
[5] F. Acernese *et al.* (The Virgo Collaboration), Phys. Rev. Lett. **125**, 131101 (2020).
[6] J. D. Teufel, T. Donner, M. A. Castellanos-Beltran, J. W. Harlow, and K. W. Lehnert, Nat. Nanotechnol. **4**, 820 (2009).
[7] G. Anetsberger, E. Gavartin, O. Arcizet, Q. P. Unterreithmeier, E. M. Weig, M. L. Gorodetsky, J. P.

Kotthaus, and T. J. Kippenberg, Phys. Rev. A **82**, 061804(R) (2010).
[8] K. W. Murch, K. L. Moore, S. Gupta, and D. M. Stamper-Kurn, Nat. Phys. **4**, 561 (2008).
[9] T. P. Purdy, R. W. Peterson, and C. A. Regal, Science **339**, 801 (2013).
[10] J. D. Teufel, F. Lecocq, and R. W. Simmonds, Phys. Rev. Lett. **116**, 013602 (2016).
[11] J. Cripe, N. Aggarwal, R. Lanza, A. Libson, R. Singh, P. Heu, D. Follman, G. D. Cole, N. Mavalvala, and T. Corbitt, Nature (London) **568**, 364 (2019).
[12] J. Cripe, T. Cullen, Y. Chen, P. Heu, D. Follman, G. D. Cole, and T. Corbitt, Phys. Rev. X **10**, 031065 (2020).
[13] S. Schreppler, N. Spethmann, N. Brahms, T. Botter, M. Barrios, and D. M. Stamper-Kurn, Science **344**, 1486 (2014).
[14] D. J. Wilson, V. Sudhir, N. Piro, R. Schilling, A. Ghadimi, and T. J. Kippenberg, Nature (London) **524**, 325 (2015).
[15] M. Rossi, D. Mason, J. Chen, Y. Tsaturyan, and A. Schliesser, Nature (London) **563**, 53 (2018).
[16] H. J. Kimble, Y. Levin, A. B. Matsko, K. S. Thorne, and S. P. Vyatchanin, Phys. Rev. D **65**, 022002 (2001).
[17] S. Vyatchanin and E. Zubova, Phys. Lett. A **201**, 269 (1995).
[18] J. B. Hertzberg, T. Rocheleau, T. Ndukum, M. Savva, A. A. Clerk, and K. C. Schwab, Nat. Phys. **6**, 213 (2010).
[19] J. Suh, A. J. Weinstein, C. U. Lei, E. E. Wollman, S. K. Steinke, P. Meystre, A. A. Clerk, and K. C. Schwab, Science **344**, 1262 (2014).
[20] I. Shomroni, L. Qiu, D. Malz, A. Nunnenkamp, and T. J. Kippenberg, Nat. Commun. **10**, 2086 (2019).
[21] V. B. Braginsky, Y. I. Vorontsov, and K. S. Thorne, Science **209**, 547 (1980).
[22] G. Vasilakis, H. Shen, K. Jensen, M. Balabas, D. Salart, B. Chen, and E. S. Polzik, Nat. Phys. **11**, 389 (2015).
[23] Y. Chen, S. L. Danilishin, F. Y. Khalili, and H. Müller-Ebhardt, Gen. Relativ. Gravit. **43**, 671 (2011).
[24] R. S. Bondurant, Phys. Rev. A **34**, 3927 (1986).
[25] S. Chelkowski, H. Vahlbruch, B. Hage, A. Franzen, N. Lastzka, K. Danzmann, and R. Schnabel, Phys. Rev. A **71**, 013806 (2005).
[26] E. Oelker, T. Isogai, J. Miller, M. Tse, L. Barsotti, N. Mavalvala, and M. Evans, Phys. Rev. Lett. **116**, 041102 (2016).
[27] L. McCuller, C. Whittle, D. Ganapathy, K. Komori, M. Tse, A. Fernandez-Galiana, L. Barsotti, P. Fritschel, M. MacInnis, F. Matichard, K. Mason, N. Mavalvala, R. Mittleman, H. Yu, M. E. Zucker, and M. Evans, Phys. Rev. Lett. **124**, 171102 (2020).
[28] Y. Zhao *et al.*, Phys. Rev. Lett. **124**, 171101 (2020).
[29] E. S. Polzik and K. Hammerer, Ann. Phys. (Berlin) **527**, A15 (2015).
[30] C. B. Møller, R. A. Thomas, G. Vasilakis, E. Zeuthen, Y. Tsaturyan, M. Balabas, K. Jensen, A. Schliesser, K. Hammerer, and E. S. Polzik, Nature (London) **547**, 191 (2017).
[31] M. Tsang and C. M. Caves, Phys. Rev. Lett. **105**, 123601 (2010).
[32] M. H. Wimmer, D. Steinmeyer, K. Hammerer, and M. Heurs, Phys. Rev. A **89**, 053836 (2014).
[33] D. Steinmeyer, Subsystems for all-optical coherent quantum-noise cancellation, Ph.D. thesis, Gottfried Wilhelm Leibniz Universität Hannover, 2019.
[34] M. J. Collett and C. W. Gardiner, Phys. Rev. A **30**, 1386 (1984).
[35] C. W. Gardiner and C. M. Savage, Opt. Commun. **50**, 173 (1984).
[36] C. Fabre, E. Giacobino, A. Heidmann, L. Lugiato, S. Reynaud, M. Vadacchino, and W. Kaige, Quantum Opt. **2**, 159 (1990).
[37] L.-A. Wu, M. Xiao, and H. J. Kimble, J. Opt. Soc. Am. B **4**, 1465 (1987).
[38] T. Aoki, G. Takahashi, and A. Furusawa, Opt. Express **14**, 6930 (2006).
[39] S. Dwyer *et al.*, Opt. Express **21**, 19047 (2013).
[40] J. Junker, D. Wilken, E. Huntington, and M. Heurs, Opt. Express **29**, 6053 (2021).
[41] A. E. Dunlop, E. H. Huntington, C. C. Harb, and T. C. Ralph, Phys. Rev. A **73**, 013817 (2006).
[42] C. W. Gardiner and M. J. Collett, Phys. Rev. A **31**, 3761 (1985).
[43] U. Leonhardt, *Measuring the Quantum State of Light* (Cambridge University Press, Cambridge, England, 1997).
[44] G. Adesso, S. Ragy, and A. Lee, Open Syst. Inf. Dyn. **21** (2014).
[45] M. Mehmet, S. Ast, T. Eberle, S. Steinlechner, H. Vahlbruch, and R. Schnabel, Opt. Express **19**, 25763 (2011).
[46] H. Vahlbruch, M. Mehmet, K. Danzmann, and R. Schnabel, Phys. Rev. Lett. **117**, 110801 (2016).
[47] See Supplemental Material at http://link.aps.org/supplemental/10.1103/PhysRevLett.129.033602 for animation showing the frequency-dependent rotation of the squeezed state.
[48] ET Steering Committee Editorial Team, Technical Report No. ET-0007B-20, 2020.
[49] M. Maggiore, C. V. D. Broeck, N. Bartolo, E. Belgacem, D. Bertacca, M. A. Bizouard, M. Branchesi, S. Clesse, S. Foffa, J. García-Bellido, S. Grimm, J. Harms, T. Hinderer, S. Matarrese, C. Palomba, M. Peloso, A. Ricciardone, and M. Sakellariadou, J. Cosmol. Astropart. Phys. 03 (2020) 050.